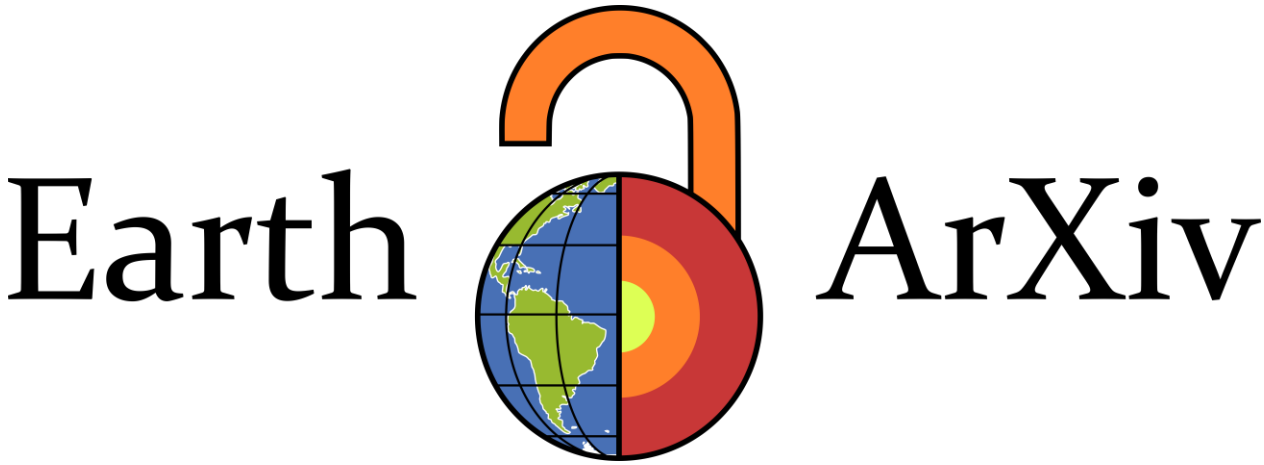

A PETROGRAPHIC P-AXIS AS AN INDEPENDENT STATE COORDINATE OF COAL ORGANIC MATTER: DECOUPLING OF ORGANIC SULFUR AND INORGANIC FE–S SUBSYSTEMS

Olga N. Shagarova

PhD in Technical Sciences, Associate Professor

National University of Science and Technology MISIS (NUST MISIS), Moscow, Russia

Email: shagarova.on@misis.ru

ORCID: 0009-0007-8195-5827

Short Description

This study proposes an architectural framework for coal organic matter in which geochemical behavior emerges from the interaction of partially independent subsystems rather than from a single maturity or redox gradient. Using a globally compiled coal dataset, we introduce the P-axis—a petrographic coordinate derived exclusively from the balance between gelified and tissue-preserved vitrinite components—and demonstrate that reproducible geochemical organization recurs along this axis across multiple basins and countries. The results show that organic sulfur, inorganic Fe–S redox, lithogenic, alkali-fluid, and rank-related subsystems exhibit distinct patterns of organization, indicating that gelification, thermal maturity, and inorganic Fe–S redox are overlapping but non-identical process systems. The framework provides a reproducible, multidimensional approach to characterizing coal organic matter architecture beyond conventional single-proxy interpretations.

A Petrographic P-Axis as an Independent State Coordinate of Coal Organic Matter: Decoupling of Organic Sulfur and Inorganic Fe–S Subsystems

Abstract

Coal geochemistry is commonly interpreted through rank, maceral composition, or redox gradients, yet these single-gradient frameworks often fail to explain the recurrent heterogeneity observed among coals of similar maturity and petrographic composition. Rather than seeking a single universal proxy of gelification, this study proposes an architectural framework in which coal organic matter is represented as a multidimensional process-space composed of partially independent subsystems, including organic sulfur, inorganic Fe–S redox, lithogenic, alkali-fluid, carbonate, phosphate, ash-source, and rank-related components.

To operationalize this architecture, we introduce the P-axis, a continuous petrographic coordinate derived exclusively from the balance between gelified (G) and tissue-preserved (T) vitrinite components, without the use of any geochemical input variables. Using a globally compiled coal dataset (WoCQI), we evaluate whether reproducible geochemical organization emerges around this petrographically defined coordinate and whether such organization can be reduced to conventional maturity measures.

The results reveal a coherent bipolar architecture. The tissue-preserved pole (T-ref) is associated with lithogenic, oxygen-rich, moisture-rich, and volatile-related signatures, whereas the gelified pole (G-ref) is characterized by organic sulfur enrichment, increasing carbonization, and a recurrent Sb–Tl–Hg–Cl–Te assemblage accompanied by alkali-fluid associations. Multiple geochemical subsystems exhibit stable and reproducible partitioning along the P-axis across different basins and countries.

Importantly, organic sulfur-associated and inorganic Fe–S-associated signals diverge along the petrographic gradient. S_organic and bio_organic_sulfur_score are consistently enriched toward G-ref, whereas S_pyritic, inorganic_FeS_redox_score, U, and V display weak, unstable, or non-polar responses. These observations indicate that gelification, thermal maturity, and inorganic Fe–S redox represent overlapping but non-identical process systems and should not be treated as interchangeable descriptors of coal state.

The P-axis is not reducible to Rmax or ash content; instead, it provides a reproducible petrographic state coordinate that recurs across multiple basins and countries. More broadly, the proposed framework shifts coal interpretation from isolated proxy variables toward quantitative characterization of coal organic matter architecture and the interactions among its constituent geochemical subsystems.

Keywords: coal geochemistry; coal petrography; organic matter architecture; gelification; P-axis; process-space analysis; organic sulfur; Fe–S redox system; coal maturity; vitrinite; compositional data analysis; state-space framework

1. INTRODUCTION

Gelification of organic matter in coals has traditionally been regarded as a petrographic indicator of anaerobic peat-forming conditions and early diagenesis, associated with the destruction of plant tissue structure and the formation of a homogenized gel-like organic matrix (Teichmüller, 1989, 1990; Diessel, 1992; Dai et al., 2020). In applied coal geochemistry, gelified states are commonly interpreted in terms of a unified redox gradient predominantly controlled by the inorganic Fe–S system, including pyritization, sulfate reduction, and the behavior of classical redox-sensitive elements such as U, V, and Mo (Jones and Manning, 1994; Ruebsam et al., 2017). However, numerous attempts to relate petrographic gelification to any universal geochemical proxy - whether a single element, elemental ratio, or integrated index - have produced contradictory and poorly reproducible results between basins and depositional systems (Hower et al., 1994; Hower and Eble, 1996; Sen, 2016; Dai et al., 2020). This suggests that gelification, as a petrographic category, may not be reducible to a single geochemical process, but instead reflects a more complex hierarchy of partially independent subsystems.

Knowledge Gap and Problem Statement

The absence of a reproducible geochemical correlate of gelification may therefore be not accidental, but fundamental. The traditional approach - searching for a single element, elemental ratio, or integrated index capable of "tracking" gelification - may be intrinsically inadequate for the nature of coal systems. Instead, gelification may represent an architectural state of the organic matrix, within which several partially independent subsystems - including organic sulfur, the inorganic Fe–S redox system, the lithogenic framework, fluid-associated elements, and rank-related parameters - are reorganized in a coordinated, but not necessarily synchronous or obligatorily coupled manner (Jones and Manning, 1994; Sen, 2016; Chou, 2012; Amrani, 2014; Dai et al., 2020).

The need to characterize coal organic matter beyond standard petrographic composition and rank has been recognized within the framework of genetic classification, particularly regarding the structural and textural features of vitrinite (Epshtein et al., 2017, 2020). These studies have demonstrated that coals with similar maceral composition and Rmax may exhibit different physical and chemical properties due to variations in the internal organization of the vitrinite matrix. However, a quantitative, petrographically defined coordinate capturing this dimension has been lacking.

Approach and Central Idea

In the present study, we propose a fundamentally different approach. Instead of searching for a single geochemical correlate of gelification, we construct a continuous petrographic state coordinate of organic matter, termed the P-axis, representing the transition from tissue preservation to gelification (tissue-to-gel transformation). The P-axis is calculated exclusively from the proportion of tissue-preserved (T) and gelified (G) vitrinite components, without the use of any geochemical variables. We then examine how different geochemical subsystems are reproducibly organized around this independent petrographic axis, including

elemental composition, sulfur forms, proximate and ultimate parameters, oxide systems, and ash-source organization. Such an approach makes it possible to distinguish the internal transformation of the organic matrix - including early biogelification processes and the associated homogenization of organic tissue - from external or late-diagenetic geochemical overprints (Teichmüller, 1989, 1990; Diessel, 1992; Casagrande, 1987; Chou, 2012; Dai et al., 2020).

The central conceptual position of this work is that the P-axis primarily captures the internal state of the organic matrix and the degree of tissue-to-gel transformation, whereas a substantial part of the classical inorganic Fe–S-associated redox proxies may instead be controlled by later or externally imposed geochemical factors, including sulfate and iron availability, changes in pore-water chemistry, and fluid-related inputs (Jones and Manning, 1994; Chou, 2012; Ruebsam et al., 2017). As we demonstrate below, this distinction explains why petrographic gelification and inorganic Fe–S-associated redox proxies may become partially decoupled along the P-axis.

Aim of the Study

The aim of this study is to test whether a petrographically defined P-axis, constructed exclusively from the ratio of tissue-preserved and gelified vitrinite components, can serve as an independent state coordinate of coal organic matter - reflecting a continuous transition from tissue preservation to gelification - around which geochemical, sulfur-related, mineral, and rank-related subsystems are reproducibly organized.

More specifically, this work examines whether petrographic gelification can be reduced to a single inorganic Fe–S-associated redox gradient, or whether it instead represents an autonomous architectural state of the organic matrix, within which organic sulfur-associated and inorganic Fe–S-associated signals may become partially decoupled (Casagrande, 1987; Jones and Manning, 1994; Chou, 2012; Amrani, 2014; Dai et al., 2020).

Working Hypotheses

H1. P-domains are reproducible across basins.

The P-axis is not interpreted as a hidden code of basin affinity: similar P-states should recur across different basins and countries. This hypothesis is evaluated through analysis of the distribution of the five global P-domains relative to the basin and country structure of the dataset, as well as through basin-stratified permutation analysis.

H2. A coherent geochemical architecture is organized around the P-axis.

If the P-axis reflects the internal state of organic matter, T_ref and G_ref should differ not by isolated elements or individual proxy indicators, but by a coordinated reorganization of element-associated, proximate/ultimate, oxide-related, and sulfur-related subsystems.

H3. Organic sulfur-associated and inorganic Fe–S-associated signals diverge relative to the P-axis.

The key prediction is that S_organic and bio_organic_sulfur_score should exhibit systematic behavior relative

to the P-axis distinct from that of S_pyritic, Fe_2O_3, and inorganic_FeS_redox_score, indicating different degrees of association with the P-axis.

H4. The P-axis is not reducible to Rmax or ash content.

If the P-axis represents an independent petrographic coordinate, the observed P-configuration should not be fully explained either by thermal maturity or by total ash content.

Research Objectives

To achieve the stated aim and test the proposed hypotheses, the following objectives are addressed:

- To construct a continuous petrographic P-axis based on tissue-preserved (T) and gelified (G) vitrinite components without the use of geochemical variables.
- To evaluate the robustness of the P-axis with respect to the choice of stabilizing constant, the strict form of the model, and calculation parameterization.
- To identify global P-domains and assess their reproducibility across different basins.
- To calculate standardized Z-contrasts between T_ref and G_ref and identify elements consistently associated with the tissue-preserved and gelified poles.
- To evaluate the reorganization of proximate, ultimate, and oxide-related parameters along the P-axis.
- To test whether the observed P-configuration can be explained solely by thermal maturity (Rmax) or total ash content.
- To separate organic sulfur-associated and inorganic Fe–S-associated subsystems and evaluate their partial independence relative to the P-axis.
- To interpret the P-space as a multidimensional process-space organization of organic matter states rather than as a single-proxy redox indicator.

2. MATERIALS AND METHODS

2.1. Source Data and Dataset Structure

The study was based on a consolidated coal database compiled from the World Coal Quality Inventory (WoCQI) and related analytical datasets containing petrographic, geochemical, and technological characteristics of coal samples (Finkelman and Lovern, 2001; Tewalt et al., 2006). Unlike many global compilations integrating results from independent laboratories, the WoCQI was developed within a centralized USGS analytical program. The accompanying documentation explicitly emphasizes that the database “does not have the inter-laboratory variability that is present in many compilations,” making it particularly suitable for cross-basin comparisons (Finkelman and Lovern, 2001).

For the purposes of the present study, it was critically important that the samples used for construction of the petrographically calibrated P-axis were generated within a single analytical chain and laboratory framework. Any systematic analytical biases, if present, are therefore shared across the entire dataset rather than being randomly distributed among basins and countries. Because the analysis focuses primarily on relative

contrasts, rank relationships, bootstrap robustness, and the reproducibility of architectural states, a uniform analytical bias was considered less critical than inter-laboratory variability (Kane, 1992; Jochum and Nohl, 2008).

WoCQI represents an open-access USGS data source; the calibration table used in the present study was compiled from publicly available records following variable-name harmonization, data-type verification, and filtering based on information completeness.

The calibration dataset included 98 samples from 11 countries and multiple basin/provenance groups. Of the 98 samples, measurements of maximum vitrinite reflectance (Rmax, %) were available for 92 samples; the Rmax range was 0.31–2.94%. The dataset was not artificially balanced by basin and was not normalized by country. Basin affiliation was used not for construction of the P-axis itself, but as an independent level for testing reproducibility and evaluating basin-conditioned effects.

From the initial array of geochemical variables, elements and oxides were selected according to two criteria: a proportion of valid numerical values of at least 0.6 and a proportion of censored values below the detection limit (<LOD) not exceeding 0.5. As a result, 44 elements and 10 oxides were retained for analysis. Element concentrations in the original database were reported primarily in ppm and %, oxide data and ash values in %, and gross calorific value in either MJ/kg or Btu/lb depending on the original WoCQI record.

Values reported as <X were replaced with X/2; in total, 165 censored cells across 20 columns were substituted in this manner. Values reported as <RPT ("less than reported") were not replaced and were retained as missing values because they indicate analytical problems rather than censoring below the detection limit. Their total proportion was below 1% and did not exert a noticeable influence on the distributions or rank relationships of the analyzed variables.

Samples lacking data for the key petrographic variables T and G were excluded. For variables used only in diagnostic or validation blocks, missing values were not imputed, and analyses were performed on the subset of available observations. Rank-based statistics were preferentially employed because a substantial proportion of the geochemical variables exhibited non-normal and heteroscedastic distributions.

2.2. Construction of the Petrographic P-Axis

The central object of the study was a continuous petrographic coordinate, P, describing the position of a sample between tissue-preserved and gelified states of organic matter. It is critically important that the P-axis was constructed exclusively from petrographic parameters and did not incorporate any geochemical variables. Values of both T and G were available for all 98 samples of the calibration dataset, allowing construction of the P-axis without additional imputation of petrographic variables.

The T-component (tissue-preserved fraction) was defined as the sum of structurally preserved vitrinite microcomponents:

$$T = \text{telinite} - 1 + \text{telinite} - 2 + \text{textinite}$$

The G-component (gelified fraction) was defined as the sum of gelified components:

$$G = \text{gelinite} + \text{gelodetrinite} + \text{corpogelinite}$$

Under conditions of pronounced gelification, collodetrinite was additionally included in G. Thus, T and G reflected not the geochemical properties of the sample, but the petrographically observed balance between preserved tissue structure and homogenized gelified organic matter (Teichmüller, 1989, 1990; Diessel, 1992).

The petrographic coordinate was calculated as the logarithmic ratio of G and T:

$$P = \ln((G + \delta)/(T + \delta))$$

where δ is a stabilizing constant. In the main model, the following value was used:

$$\delta = 0.5$$

This value corresponds to the minimum petrographic counting increment and prevents division by zero, logarithmic instability at low values, and artificial hyperbolization of rare components.

Additional sensitivity analyses were performed using $\delta = 0.1$ and $\delta = 1.0$, as well as using the strict form:

$$P\_strict = \ln(G/T)$$

applied only to samples with (G>0) and (T>0). The strict P model was not used as the primary definition because it excludes samples containing zero values of T or G and may therefore artificially compress the space of extreme petrographic states. Instead, it was treated as a sensitivity check rather than a unique definition of P. Element ranking based on Z-scores remained consistent across all variants of the P-model, indicating that the inferred architectural relationships were robust to the treatment of zero values.

Negative P values correspond to dominance of tissue-preserved components ((T>G)), whereas positive values indicate dominance of the gelified matrix ((G>T)). The P-axis is interpreted as a continuous coordinate of the structural state of organic matter rather than as a geochemical redox indicator, groundwater-level proxy, or surrogate of thermal maturity.

For cross-basin analysis, the continuous P-axis was discretized into five global P-domains corresponding to quintile partitioning of the full distribution: P01 (strong T_ref), P02 (weak T transition), P03 (mixed middle), P04 (weak G transition), and P05 (strong G_ref). Domain boundaries were defined globally across the entire dataset rather than separately within individual basins. The purpose of the P-domains was not to normalize inter-basin differences, but rather to test whether similar P-states recur across different basins and countries.

In addition, two polar reference states were defined: T_ref as the lower quartile of the P distribution and G_ref as the upper quartile. These groups were used as reference poles for calculation of geochemical contrasts between tissue-preserved and gelified states.

2.2.1. Stability of P-Space and Requirements for State Coverage

Because the P-axis is interpreted as a continuous coordinate of organic matter state, the stability of the process-space architecture depends not only on the total number of samples, but also on the completeness of coverage of both polar and intermediate P-states.

For stable reconstruction of the P-architecture, it is essential that the calibration dataset:

- contains both polar states (T_ref and G_ref);
- includes a sufficient number of samples within the polar groups;
- is not extremely biased toward one pole;
- preserves continuous coverage of intermediate P-states;
- incorporates cross-basin variability.

Sensitivity analysis demonstrated that limited coverage of one of the poles, or a strong imbalance between the polar groups, may produce local variability in individual Z-contrasts and in the ranking of certain elements, although the overall P-space architecture and the direction of the principal polar associations remain preserved.

This indicates that the P-space represents an architecture-sensitive state-space model, whose stability is determined by the completeness of representation of the multidimensional state space rather than by sample size alone.

2.3. Geochemical Processing and Log-Contrast Transformation

To suppress compositional data effects and account for the lithogenic background, all elemental concentrations after <LOD processing were transformed into log-contrast variables relative to the Al–Si–Ti framework (Aitchison, 1986; for comprehensive treatments of compositional data analysis, see Pawlowsky-Glahn et al., 2015; Filzmoser et al., 2018):

$$\mathrm{lc(E)} = \log(1 + \mathrm{E}) - 1/3 \times [\log(1 + \mathrm{Al}) + \log(1 + \mathrm{Si}) + \log(1 + \mathrm{Ti})]$$

where E is the elemental concentration in the original analytical units. Al, Si, and Ti were selected as components of the lithogenic framework because their variability primarily reflects terrigenous dilution and the mineral matrix. This approach allowed analysis of relative elemental enrichment or depletion against the background of the principal lithogenic components rather than relying solely on absolute concentrations.

To test the robustness of the results to background selection, alternative log-contrast models were additionally calculated using the following frameworks: Al–Si, Al–Ti, Si–Ti, Al–Si–Ti–Zr, Al–Si–Ti–Sc, and Al–Si–Ti–Zr–Sc. Element rankings based on Z-scores were compared among background models using Spearman rank correlation. High rank consistency was interpreted as evidence that the observed geochemical organization was not an artifact of arbitrary lithogenic-background selection.

2.4. Standardized Contrasts and Bootstrap Robustness

To evaluate differences between the polar petrographic states, standardized contrasts between G_ref and T_ref were calculated as:

$$Z = (\mu\_G\_ref - \mu\_T\_ref) / SD\_pooled$$

where SD_pooled is the pooled standard deviation:

$$SD\_pooled = sqrt\{[(n\_G - 1)SD\_G^2 + (n\_T - 1)SD\_T^2] / (n\_G + n\_T - 2)\}$$

Positive Z values indicate enrichment in G_ref, whereas negative values indicate association with T_ref. The absolute magnitude |Z| was used as a measure of contrast strength. Elements with $|Z| \geq 0.8$ were treated as candidates for interpretation, whereas elements with $|Z| \geq 1.0$ were considered to exhibit strong contrasts. These thresholds were used exclusively for ranking and preparation of result tables and were not interpreted as formal statistical significance criteria. Statistical robustness of both contrast direction and magnitude was evaluated separately using bootstrap confidence intervals.

Contrast robustness was assessed by bootstrap resampling with 2000 independent iterations (Efron and Tibshirani, 1993). During each iteration, the T_ref and G_ref groups were resampled with replacement, after which the Z-contrast was recalculated. For each element, a 95% bootstrap confidence interval was estimated using the percentile method based on the 2.5th and 97.5th percentiles of the bootstrap distribution. Percentile bootstrap intervals were selected because the analysis did not assume Gaussian distributions of effect sizes. A contrast was considered robust if the confidence interval did not cross zero.

Additional robustness checks were performed by varying the P-model, modifying the lithogenic background, and applying jackknife exclusion of 10% of the samples. Median-based contrasts were used as an additional control for outlier influence; agreement between rankings derived from mean-based and median-based contrasts indicated that the principal results were not controlled by isolated extreme values.

2.5. Control of Basin Effects and Thermal Maturity

Because samples originating from the same basin may share similar formation conditions, there was a risk of falsely interpreting the P-axis as a hidden basin effect. To evaluate this possibility, basin-stratified permutation analysis was performed, in which T_ref and G_ref labels were randomly permuted only within individual basins while preserving the overall structure of the dataset. For each element, 500 permutations were calculated. If the observed Z-contrast exceeded 95% of the permuted values, the effect was interpreted as not reducible to a basin-conditioned artifact.

In addition, P-domain × basin and P-domain × country matrices were constructed. These matrices were used not for basin normalization, but for testing the cross-basin recurrence of similar P-states. The occurrence of the same P-domain across multiple basins and countries was interpreted as evidence that the P-axis does not represent a simple code of basin affinity.

Because thermal maturity may influence both maceral composition and geochemistry, an additional

analysis was performed to test whether the P-axis could represent a hidden surrogate of coal rank. For this purpose, measured Rmax values and compositional rank proxies - including fixed carbon, volatile matter, gross calorific value (MJ/kg or Btu/lb), and O/H ratios - were used.

To evaluate relationships between P and geochemical variables while controlling for Rmax, an approximation of partial Spearman correlation was implemented through rank residualisation. Ranks of variable x (P) and variable y (element log-contrast) were separately regressed against the rank of the control variable z (Rmax), after which Pearson correlation was calculated between the residuals. The analysis was performed only for triplets with $n \geq 8$ after removal of missing values. This procedure was used as a diagnostic tool rather than as a strict test of conditional independence.

An important principle of the analysis was the explicit separation between the P-axis and the maturity axis. The Rmax-axis was constructed exclusively from Rmax values. When Rrandom values were available, they were treated separately and were not merged with Rmax. This prevented different maturity indicators from collapsing into a single implicit variable and allowed assessment of which elements were associated primarily with petrographic gelification and which were associated predominantly with thermal maturity.

2.6. Process-Space Architecture

Instead of searching for individual universal elemental proxies, an architectural approach was adopted in which each sample was represented as a position within a multidimensional process space. In the present study, process space is defined as a system of operational coordinates reflecting different partially independent geochemical subsystems, including organic sulfur, Fe–S redox, lithogenic, carbonate, alkali-fluid, phosphate, and rank-related subsystems.

All process-space coordinates were scaled using robust scaling:

$$\text{scaled} = (x - q05)/(q95 - q05)$$

where q05 and q95 correspond to the 5th and 95th percentiles, respectively. The use of percentile-based scaling instead of minimum and maximum values reduces the influence of extreme outliers and provides more stable calibration of the coordinates. Values outside the calibrated range were clipped:

$$\text{scaled} < 0 \rightarrow 0; \quad \text{scaled} > 1 \rightarrow 1$$

Importantly, scaling was performed at the level of individual components rather than on already averaged raw composite scores. Thus, each component was first scaled using its own q05 and q95 values, and only afterward was the corresponding process score calculated as a mean value. This prevented variables with larger numerical ranges from dominating the resulting coordinates and ensured comparability among subsystems.

The scaling parameters were fixed using the calibration dataset and stored in the JSON file process_space_calibration.json. This allowed projection of new samples into the same process space without

recalibration and without modification of the original reference boundaries.

Table 1. Principal process-space coordinates

Coordinate	Components	Interpretation
organic_S	S_organic	increased association with organic sulfur / organic matter
redox	Fe_2O_3, SO_3, S_pyritic, S_sulfate	Fe–S and sulfur-form redox organization
detrital	ash, ash_525C, ash_750C, SiO_2, Al_2O_3, TiO_2	terrigenous / clay-ash contribution
carbonate	CaO, MgO	carbonate mineralization
alkali_fluid	Na_2O, K_2O	alkali-fluid or saline contribution
phosphate	P_2O_5	phosphate contribution
rank_Rmax	Rmax	independent optical maturity
rank_proxy	fixed carbon, C, gross calorific value	auxiliary compositional maturity
low_rank_proxy	volatile matter, O, H, moisture	low-rank / volatile / oxygen-rich tendency
rank (composite)	Rmax when available, otherwise rank_proxy	technical maturity coordinate for projection

The rank_Rmax coordinate was used as an independent measure of optical maturity. The rank_proxy coordinate served as an auxiliary compositional maturity estimate based on fixed carbon, C, and gross calorific value. These coordinates were preserved separately, whereas the composite rank coordinate was used only as a technical projection coordinate when Rmax was unavailable. The low_rank_proxy coordinate was also retained separately because it reflects the opposite side of the maturity spectrum - elevated volatility, oxygen content, and moisture typical of lower-rank coals.

Process-space coordinates were interpreted as operational descriptors of multidimensional geochemical organization rather than as direct measurements of specific geological mechanisms. Accordingly, the terms redox, carbonate, alkali_fluid, and phosphate are used as names of coordinates and subsystems rather than as statements of a single causal process.

2.7. Separation of Organic Sulfur and Inorganic Fe–S Subsystems

Particular attention was devoted to separating two potentially independent sulfur-related subsystems. The inorganic Fe–S pathway included S_pyritic, Fe_2O_3, SO_3, U, V, and Mo and was interpreted as a subsystem primarily associated with pyritization, Fe–S mineral associations, and sulfur-form redox organization (Jones and Manning, 1994; Chou, 2012; Ruebsam et al., 2017). The organic sulfur pathway was centered on S_organic; additionally, Tl, Sb, Hg, and Cl were analyzed as elements empirically associated with G_ref and S_organic within the present calibration dataset.

These elements are not interpreted as universal markers of the organic sulfur pathway. In the present study, they are treated as an observed association within the calibration dataset requiring further validation using independent datasets. Such an approach was necessary to avoid replacing architectural analysis with the search for a new single proxy.

For each sample, two composite indices were calculated:

$$\text{bio\_organic\_sulfur\_score} = \text{scaled}(\text{S\_organic})$$

$$\text{inorganic\_FeS\_redox\_score} = \text{mean}[\text{scaled}(Fe_2O_3), \text{scaled}(SO_3), \text{scaled}(\text{S\_pyritic}), \text{scaled}(\text{S\_sulfate})]$$

Subsequently, Z-contrasts between T_ref and G_ref were analyzed for these indices together with bootstrap confidence intervals and their relative balance:

$$\text{balance} = \text{bio\_organic\_sulfur\_score} / \text{inorganic\_FeS\_redox\_score}$$

The purpose of this analytical block was to determine whether the organic sulfur and inorganic Fe–S subsystems remain coupled along the P-axis or are capable of diverging among P-domains, basins, and individual samples.

2.8. Ash-Source Decomposition and Mineral Subsystems

In the present study, ash content was treated not as a single parameter but as an ash-source decomposition framework incorporating several potentially independent subsystems. This approach was necessary because similar total ash contents may reflect fundamentally different geochemical configurations, including terrigenous input, carbonate mineralization, pyritization, alkali-saline contributions, or phosphate associations.

Table 2. Ash-source decomposition framework

Subsystem	Indicators	Interpretation
lithogenic	Al, Si, Ti, Zr, Sc	terrigenous / clay-related contribution
carbonate	CaO, MgO	carbonate mineralization
Fe–S	Fe_2O_3, SO_3, S_pyritic	pyritization and Fe–S processes
alkali/salt	Na_2O, K_2O, Cl	alkali-fluid or saline contribution
phosphate	P_2O_5	phosphate contribution

Ash-source decomposition was used as an additional interpretative layer within the process-space framework. It allowed differentiation between cases in which G_ref was associated predominantly with organic sulfur enrichment and cases in which gelified or transitional states were accompanied by pyritization, carbonate input, phosphate mineralization, or elevated lithogenic background.

2.9. Computational Implementation and Reproducibility

All calculations were performed in Python using the pandas, numpy, scipy, and matplotlib libraries. The principal computational pipeline included construction of multiple P-models, identification of P-domains and polar groups, log-contrast transformation, calculation of standardized contrasts, bootstrap analysis, sensitivity testing with respect to lithogenic background and P-model selection, basin-stratified permutation analysis, separation of the P- and Rmax-axes, OXPROX validation, process-space calibration, and generation of graphical outputs.

Principal component analysis (PCA) was used exclusively for exploratory visualization of

multidimensional process-space organization. PCA was not employed for hypothesis testing or statistical inference but served only as a low-dimensional representation of process-space coordinate structure.

The principal analysis script was:

calibrate_coal_gelification_multimodel_plus_oxides_FINAL_method_corrected_OXPROX_PDOMAIN_REDOX_PATCHED.py

Process-space calibration parameters were stored in the file process_space_calibration.json. The complete source code, JSON calibration files, result tables, bootstrap confidence intervals, sensitivity analyses, P-domain × basin/country matrices, and supplementary graphical materials are provided in the Supplementary Materials.

The complete computational workflow, calibration files, supplementary tables, and reproducibility package have been deposited in Zenodo and are publicly accessible via DOI: https://doi.org/10.5281/zenodo.20440805

3. RESULTS

3.1. Stability of the P-Axis and P-Models

For the calibration dataset consisting of 98 samples, the following petrographic coordinate was calculated:

$$P = \ln((G + 0.5)/(T + 0.5))$$

where T represents the sum of tissue-preserved vitrinite microcomponents and G represents the sum of gelified components. The P-axis was constructed exclusively from petrographic parameters and did not incorporate geochemical variables.

Sensitivity analysis demonstrated that variation of the stabilizing constant (δ) did not alter the overall structure of the P-space. For all three stabilized models (δ = 0.1, 0.5, and 1.0), P-values were calculated for all 98 samples. The strict form:

$$P\_strict = \ln(G/T)$$

applicable only when G > 0 and T > 0, was defined for 91 samples. Despite exclusion of 7 samples, the strict model preserved similar median and quartile characteristics.

Table 3. Stability of P-distribution under different model variants

P-model	n	min	median	max	n T_ref	n G_ref
P_δ=0.1	98	−1.35	1.10	6.86	25	25
P_δ=0.5	98	−1.04	1.08	5.26	25	25
P_δ=1.0	98	−0.88	1.06	4.57	25	25
P_strict	91	−1.47	1.07	5.49	23	23

In the principal model (P_δ=0.5), the lower quartile of the distribution was used as T_ref, whereas the

upper quartile was used as G_ref. Each group contained 25 samples, while the intermediate region contained 48 samples. The stability of polar-group sizes across different δ values indicates that the separation into T_ref and G_ref is not an artifact of a specific pseudocount selection.

Element rankings based on Z-scores also remained stable across different P-models: rank agreement between model variants exceeded $\rho > 0.95$. Therefore, subsequent geochemical contrasts can be interpreted as reflecting a stable petrographic organization rather than a technical artifact of P-formula parameterization.

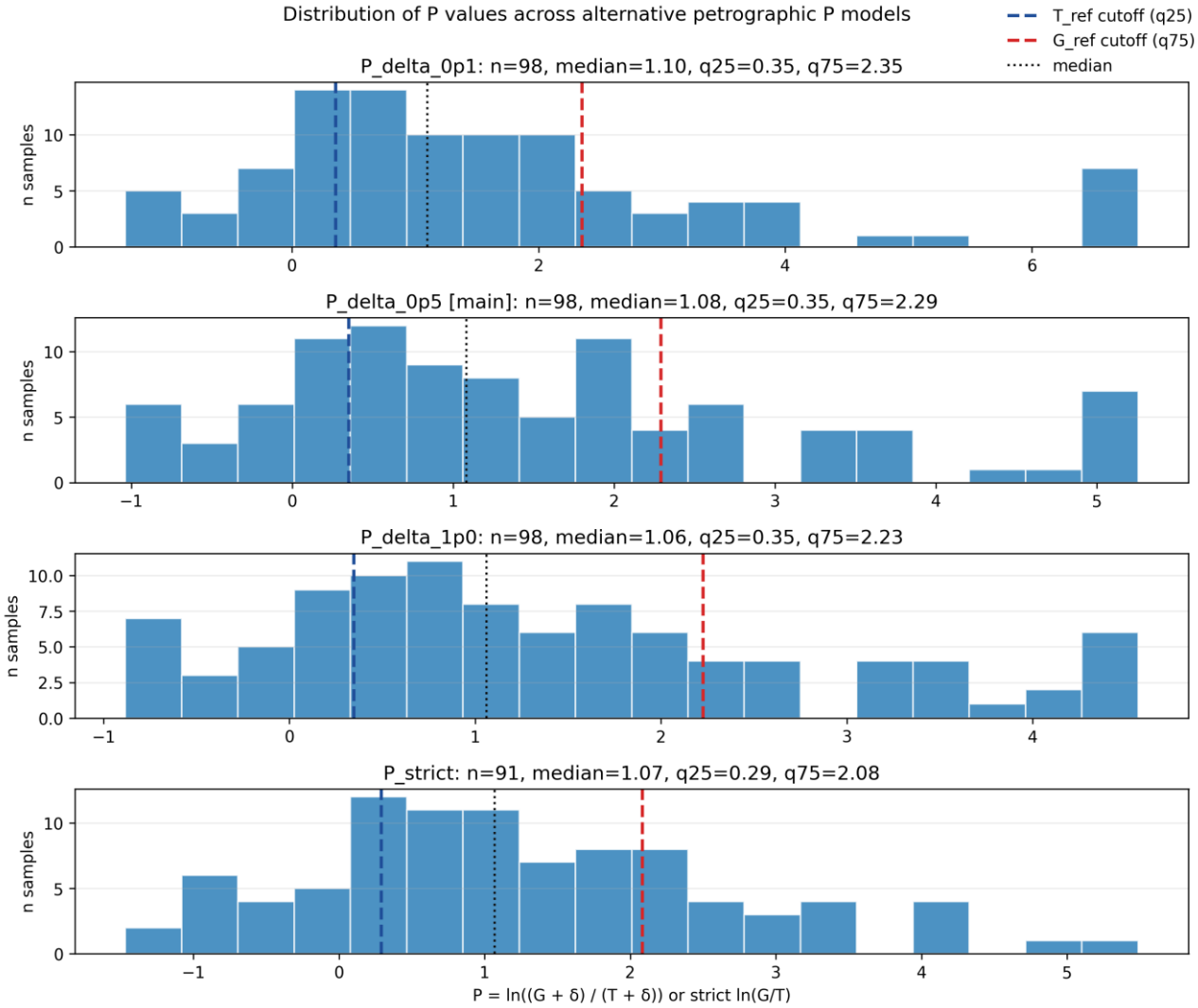

Figure 1. Distribution of P values for the P_δ=0.1, P_δ=0.5, P_δ=1.0, and P_strict models showing the positions of T_ref and G_ref.

3.2. Cross-Basin Recurrence of P-Domains

The continuous P-axis was subdivided into five global P-domains corresponding to quintile partitioning of the full distribution. These domains do not represent local groups restricted to individual basins; instead, each domain is represented by multiple basins and countries.

Table 4. Cross-basin recurrence and petrographic characteristics of P-domains

P-domain	n	n basins	n countries	P median	T median	G median	Rmax median
P01 strong T_ref	20	6	4	−0.33	4.8	2.2	0.80
P02 weak T transition	19	8	6	0.49	23.0	38.6	0.67
P03 mixed middle	20	11	7	1.08	11.7	38.4	0.75
P04 weak G transition	19	9	5	1.97	5.8	45.4	1.11
P05 strong G_ref	20	7	5	3.84	1.02	83.5	1.97

The transition from P01 to P05 is accompanied by the expected petrographic reorganization: median T values decrease whereas median G values increase. The most telinite-rich domain, P01, includes samples from 6 basins and 4 countries. The most strongly gelified domain, P05, includes samples from 7 basins and 5 countries. The intermediate domain P03 shows the broadest representation, encompassing 11 basins and 7 countries.

These results indicate that the P-domains possess genuine petrographic significance and do not simply represent geographic groupings. Basin conditions evidently influence sample distribution along the P-axis; however, similar P-states recur across independent geological systems. Accordingly, the P-axis can be characterized as basin-conditioned, but not basin-defined.

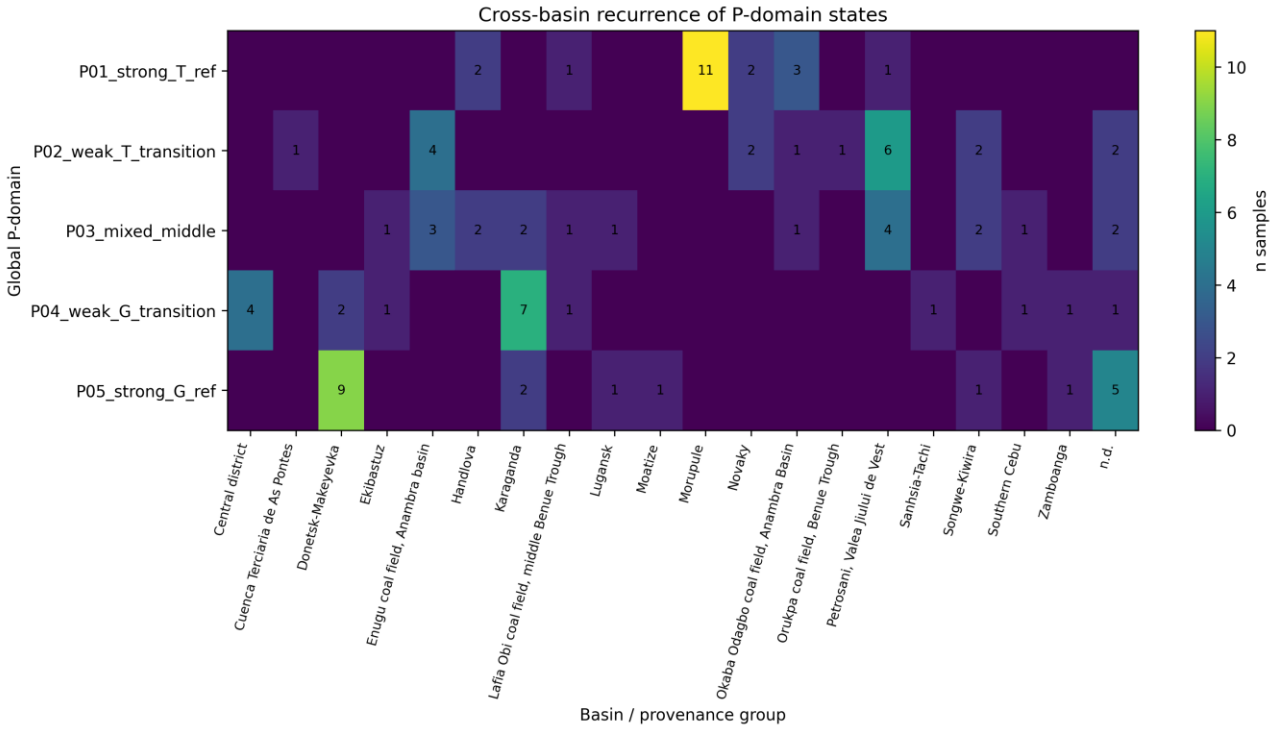

Figure 2. P-domain × basin matrix showing recurrence of P-domains among basins.

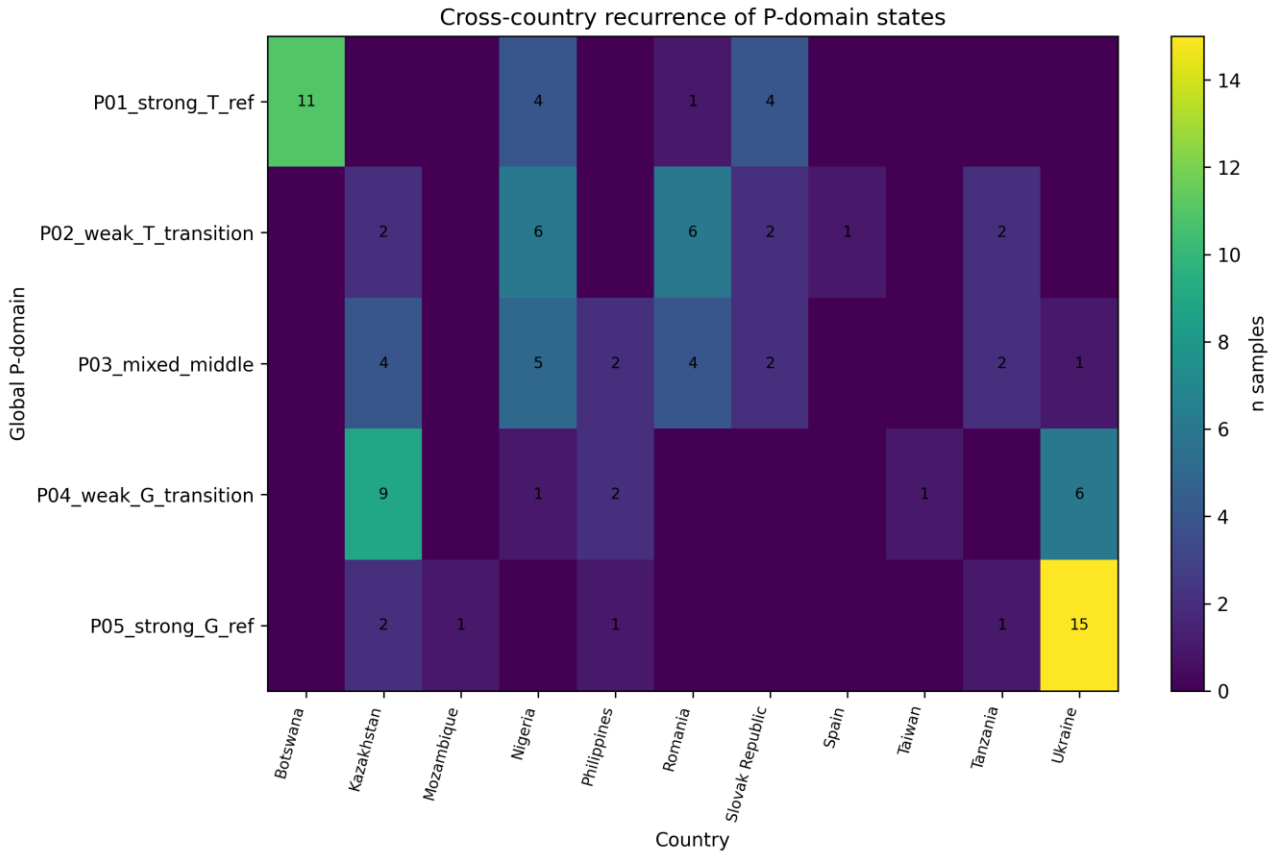

Figure 3. P-domain × country matrix showing recurrence of P-domains among countries.

3.3. Bipolar Elemental Architecture of the P-Axis

Standardized contrasts between G_ref and T_ref revealed a pronounced bipolar geochemical organization. The T-side is associated predominantly with a lithogenic-tissue signal, whereas the G-side is associated with sulfur-organic and fluid-associated signals.

On the telinite-rich side, the strongest negative Z-contrasts were observed for Th, Al, Ba, B, and Cr. On the gelified side, the strongest positive contrasts were observed for Sb, Tl, Hg, K, Cl, Te, Mo, P, Na, and Bi.

Table 5. Standardized contrasts between G_ref and T_ref for elements with |Z| ≥ 0.8

Element	Z-score	Direction	95% bootstrap CI	Robustness
Sb	+1.71	G_ref	[1.19, 2.44]	robust
Tl	+1.47	G_ref	[0.95, 2.12]	robust
Th	−1.46	T_ref	[−2.26, −0.86]	robust
Al	−1.38	T_ref	[−2.08, −0.84]	robust
Hg	+1.28	G_ref	[0.87, 1.82]	robust
K	+1.21	G_ref	[0.58, 2.16]	robust
Cl	+1.19	G_ref	[0.56, 2.13]	robust

Element	Z-score	Direction	95% bootstrap CI	Robustness
Ba	−1.17	T_ref	[−1.94, −0.62]	robust
Te	+1.16	G_ref	[0.63, 1.99]	robust
B	−1.13	T_ref	[−1.83, −0.58]	robust
Mo	+1.08	G_ref	[0.46, 2.13]	robust
P	+1.07	G_ref	[0.46, 2.05]	robust
Na	+1.06	G_ref	[0.44, 1.96]	robust
Bi	+1.05	G_ref	[0.45, 1.94]	robust
Be	+0.96	G_ref	[0.42, 1.70]	robust
Cr	−0.90	T_ref	[−1.73, −0.29]	robust
Fe	+0.86	G_ref	[0.35, 1.44]	robust

This structure cannot be reduced to isolated elements. The poles of the P-axis differ through two coherent assemblages of features: the T-side is characterized by a lithogenic-tissue association, whereas the G-side is characterized by sulfur-organic, chalcophile, and fluid-associated associations. Importantly, the strongest G-side effects are not observed for the classical U–V–Mo redox assemblage, but rather for the Sb–Tl–Hg–Cl–Te group together with Mo, Na, K, and Bi.

Neither U nor V belongs to the stable core of the G-side architecture. For U, the effect size was weak ($Z = 0.27$) and the confidence interval crossed zero; V likewise showed a weak and unstable effect. Already at the level of elemental contrasts, these results indicate that the P-axis does not coincide with a simple classical inorganic redox assemblage.

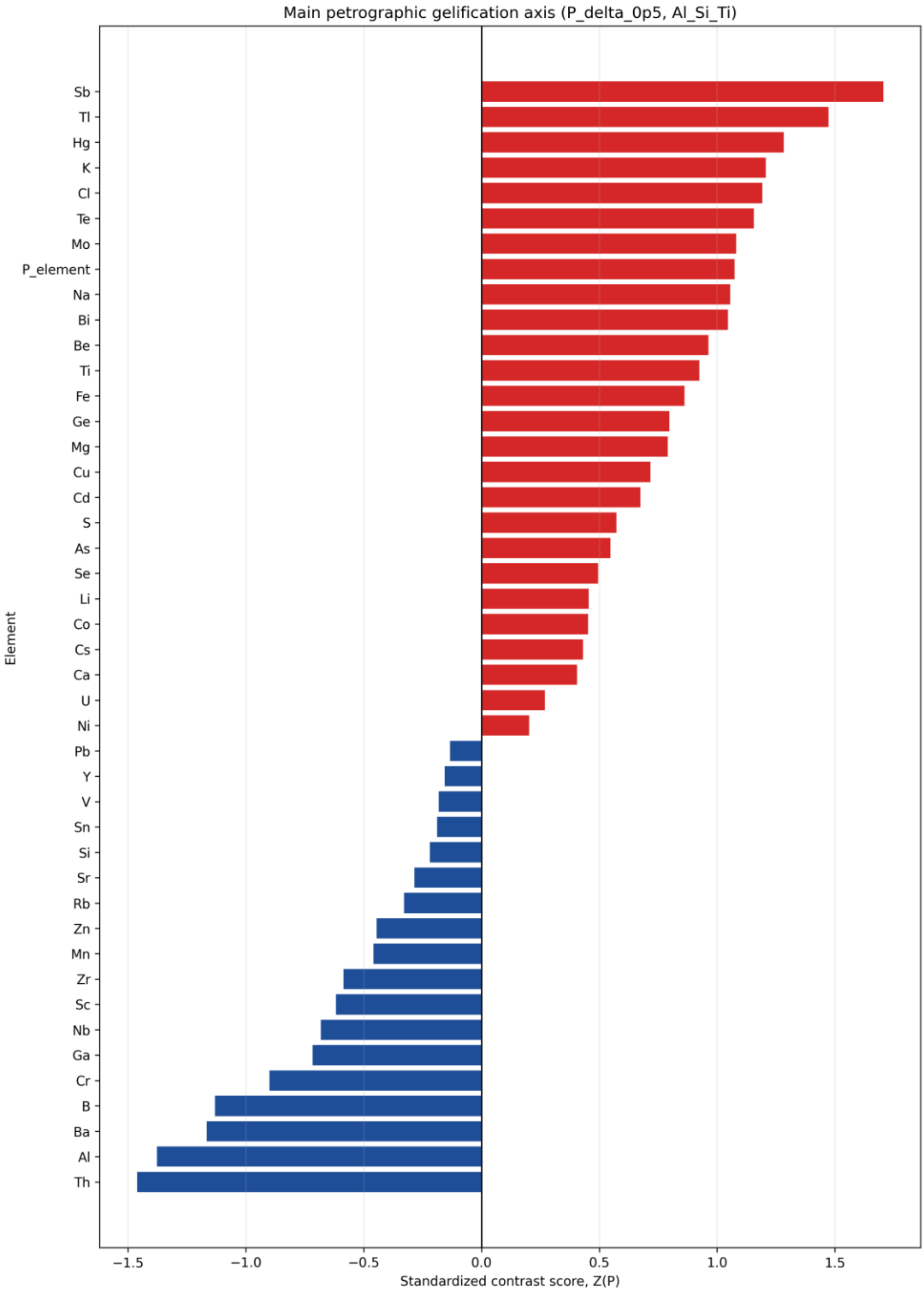

Figure 4. Ranked Z-contrasts between G_ref and T_ref for the principal model (P_δ=0.5).

3.4. Reorganization of Proximate, Ultimate, and Oxide Parameters Along the P-Axis

The P-axis is associated not only with systematic changes in elemental geochemistry, but also with coordinated reorganization of proximate, ultimate, and oxide-related parameters. This observation is

particularly important because it demonstrates that the P-axis reflects the overall state of organic matter rather than merely an isolated elemental signal.

The T-side is characterized by elevated oxygen content, moisture, volatile matter, and lithogenic-oxide parameters. In contrast, the G-side is characterized by elevated C, fixed carbon, calorific value, rank_proxy_score, and S_organic.

Table 6. Contrasts of proximate, ultimate, and oxide-related parameters between G_ref and T_ref

Parameter	Z(G_ref – T_ref)	95% bootstrap CI	Direction
O	−2.36	[−3.58, −1.71]	lower in G_ref
moisture_volatile_score	−2.27	[−3.23, −1.60]	lower in G_ref
moisture_total	−2.11	[−3.00, −1.54]	lower in G_ref
air_dry_loss	−2.02	[−3.09, −1.39]	lower in G_ref
volatile	−1.51	[−2.25, −0.95]	lower in G_ref
lithogenic_oxide_score	−1.02	[−1.93, −0.44]	lower in G_ref
ash	−0.91	[−1.64, −0.35]	lower in G_ref
SO3	−0.61	[−1.27, −0.06]	lower in G_ref
S_organic	+0.62	[0.07, 1.33]	higher in G_ref
bio_organic_sulfur_score	+0.71	[0.15, 1.41]	higher in G_ref
H	+0.76	[0.19, 1.50]	higher in G_ref
calorific_MJ_kg	+1.00	[0.81, 2.70]	higher in G_ref
N	+1.46	[0.97, 2.10]	higher in G_ref
fixed_carbon	+1.93	[1.47, 2.70]	higher in G_ref
C	+1.96	[1.38, 3.06]	higher in G_ref
calorific_Btu_lb	+1.98	[1.38, 2.99]	higher in G_ref
rank_proxy_score	+2.09	[1.51, 2.97]	higher in G_ref

These results indicate that the G-side is associated with a more carbon-rich and energetically concentrated state of organic matter, whereas the T-side is associated with a more oxygen-rich, moisture-rich, and volatile state. Importantly, the increase of rank_proxy_score on the G-side does not imply that the P-axis is fully reducible to maturity; rather, the P-axis is accompanied by maturity-related changes without being exhausted by them.

The lithogenic-oxide component is shifted toward the T-side: lithogenic_oxide_score, ash, TiO_2, and Al_2O_3 are lower in G_ref. This observation is important for subsequent interpretation because the P+ state is not a high-ash state and therefore cannot be explained solely by total ash content.

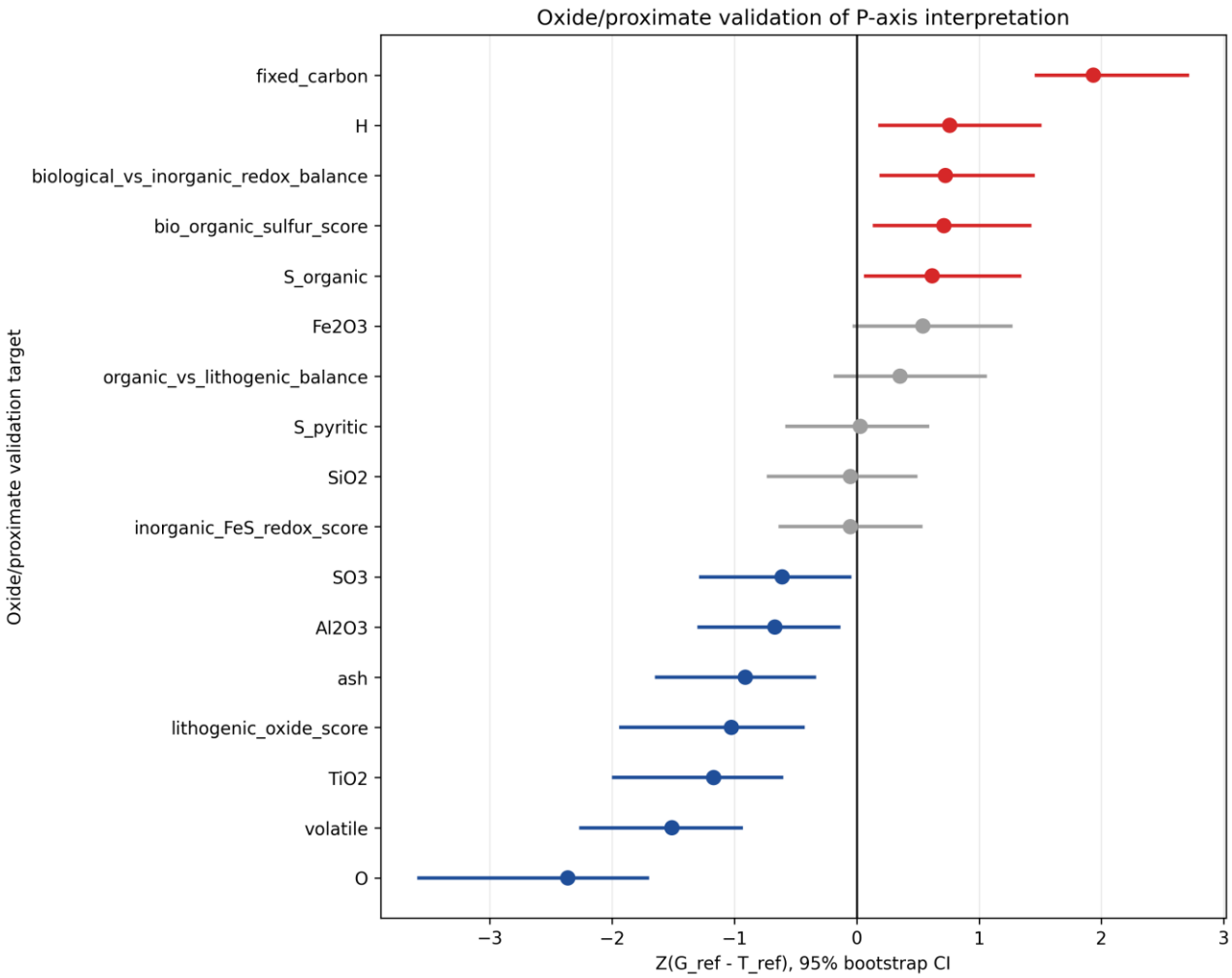

Figure 5. Changes in proximate, ultimate, and oxide-related parameters between T_ref and G_ref.

3.5. The P-Axis Is Not Reducible to Rmax or Ash Content

Comparison between Z(P) and Z(Rmax) demonstrates that the P-axis is partially associated with maturity but cannot be reduced to Rmax alone. If the P-axis merely represented a maturity axis, the strongest P-signals would be expected to coincide with the strongest Rmax-signals. However, this pattern is not observed.

Several elements display strong contrasts along the P-axis while exhibiting only weak or moderate contrasts along the Rmax-axis. These include Sb, Tl, Hg, K, Te, Mo, P, Na, and Bi. In contrast, some variables such as B and Li exhibit stronger relationships with Rmax or mixed P/rank signals.

Table 7. Examples of contrasting elemental behavior along the P-axis and Rmax-axis

Element	Z(P)	Z(Rmax)	Interpretation
Sb	+1.71	+0.63	predominantly P-related signal
Tl	+1.47	+0.61	predominantly P-related signal
Hg	+1.28	+0.68	predominantly P-related signal
K	+1.21	+0.04	predominantly P-related signal
Te	+1.16	+0.22	predominantly P-related signal
Mo	+1.08	+0.25	predominantly P-related signal
P	+1.07	+0.08	predominantly P-related signal
Na	+1.06	−0.10	predominantly P-related signal
Bi	+1.05	+0.10	predominantly P-related signal
Li	+0.46	+1.32	predominantly rank-related signal
B	−1.13	−2.82	combined P/rank signal
Al	−1.38	+0.13	opposite directions

Thus, thermal maturity participates in the overall architecture of the P-space but does not fully explain it.

The P-axis is likewise not reducible to ash content. Lithogenic_oxide_score and ash are lower in G_ref; however, different ash-source components behave differently. carbonate_buffer_score, oxide_sum, CaO, inorganic_FeS_redox_score, phosphate_score, and alkali_fluid_score do not exhibit the same stable polar behavior. Consequently, ash content cannot serve as a single explanatory factor because it itself represents a multicomponent subsystem.

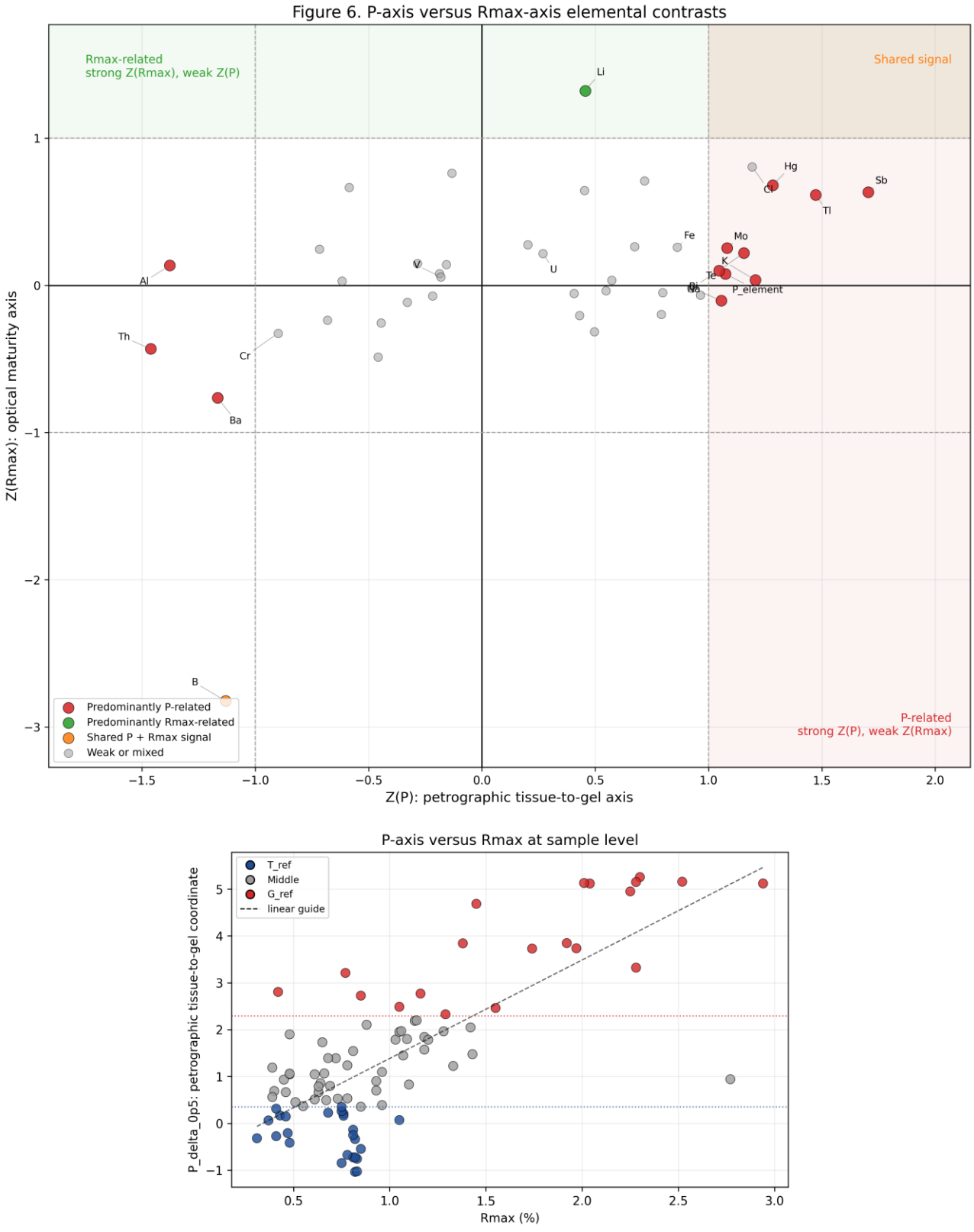

Figure 6. Comparison of Z-scores for the P-axis and the Rmax-axis. Colors indicate predominantly P-related signals, predominantly rank-related signals, shared signals, and weak or mixed effects.

3.6. OXPROX: S_organic-Associated Signal Versus Inorganic Fe–S Signal

The OXPROX analysis revealed the most important distinction within the sulfur subsystem: the S_organic-associated signal and the inorganic Fe–S signal behave differently relative to the P-axis.

S_organic and bio_organic_sulfur_score are consistently enriched in G_ref. In contrast, S_pyritic and inorganic_FeS_redox_score do not display stable contrasts between G_ref and T_ref. Fe_2O_3 exhibits a mixed effect with a confidence interval crossing zero, whereas SO_3 is even lower in G_ref.

Table 8. OXPROX analysis: S_organic-associated signal and inorganic Fe–S signal

Parameter	Z(G_ref – T_ref)	95% bootstrap CI	Interpretation
S_organic	+0.62	[0.07, 1.33]	robust G-side signal
bio_organic_sulfur_score	+0.71	[0.15, 1.41]	robust G-side signal
inorganic_FeS_redox_score	−0.05	[−0.62, 0.53]	no polar signal
S_pyritic	+0.03	[−0.57, 0.58]	no polar signal
Fe_2O_3	+0.54	[−0.02, 1.26]	confidence interval crosses zero
SO_3	−0.61	[−1.27, −0.06]	lower in G_ref
lithogenic_oxide_score	−1.02	[−1.93, −0.44]	lower in G_ref
organic_vs_inorganic_redox_balance	+0.72	[0.20, 1.44]	shifted toward S_organic in G_ref

Correlation analysis confirms the same structure. The P-axis correlates positively with bio_organic_sulfur_score ($\rho = 0.34$, $p = 0.0007$) and S_organic ($\rho = 0.33$, $p = 0.0008$), but shows no correlation with inorganic_FeS_redox_score ($\rho = -0.05$, $p = 0.62$).

Thus, the results support partial separation between the S_organic-associated signal and the inorganic Fe–S signal. This does not constitute direct evidence for a specific microbiological mechanism; rather, it demonstrates that the most stable sulfur-related signal associated with the P+ state is linked to organic sulfur rather than pyritic sulfur or an integrated Fe–S redox index.

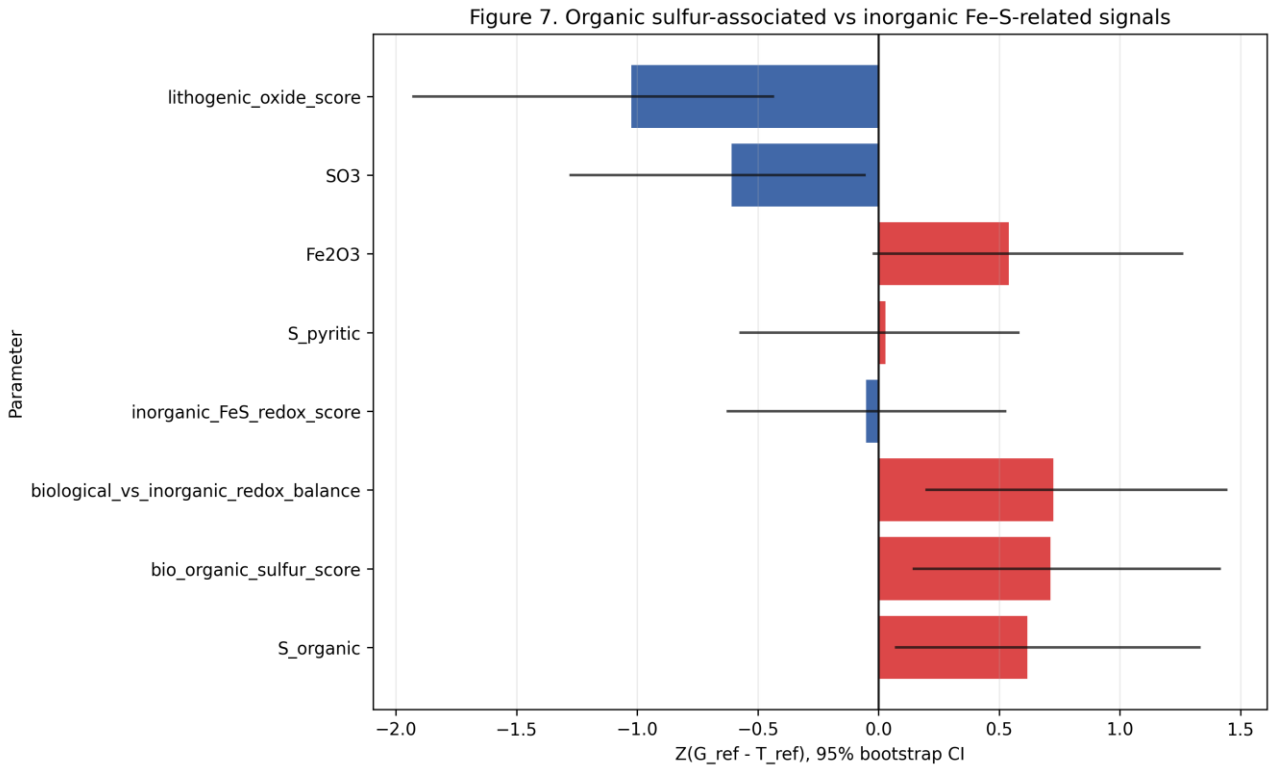

Figure 7. Comparison of S_organic-associated and inorganic Fe–S-related parameters between T_ref and G_ref.

3.7. Summary Evaluation of the Working Hypotheses

Table 9. Summary evaluation of the working hypotheses

Hypothesis	Evaluation approach	Result
H1: P-domains recur across basins	P-domain × basin/country matrices	supported by the data
H2: a coherent geochemical architecture is organized around P	Z-scores, bootstrap analysis, process scores	supported by the data
H3: S_organic-associated and inorganic Fe–S-associated signals diverge	OXPROX analysis	supported by the data
H4: P is not reducible to Rmax or ash content	Comparison with Rmax and ash-source decomposition	supported by the data

Taken together, the results demonstrate that the P-axis defines a stable space of petrographic states. These states recur across basins and are accompanied by coordinated reorganization of elemental, sulfur-related, proximate, ultimate, and oxide-related subsystems.

At the same time, the results do not support interpretation of the P-axis as a single inorganic Fe–S redox gradient. A more accurate interpretation is that the P-space organizes several partially independent subsystems, among which the S_organic-associated signal and the inorganic Fe–S signal diverge.

4. DISCUSSION

4.1. The P-Axis as a Stable Petrographic Coordinate of Organic Matter State

The present study demonstrates that the P-axis represents a stable and reproducible coordinate of organic matter state constructed independently of geochemical parameters. Unlike most traditional geochemical indices, the P-axis was calculated exclusively from the ratio of tissue-preserved and gelified vitrinite components and subsequently used as an external petrographic axis for analysis of geochemical reorganizations.

Importantly, the observed architecture does not depend on the specific mathematical form of the model. Variation of the stabilizing constant δ, as well as application of the strict form:

$$P = \ln(G/T)$$

does not produce substantial reorganization of the polar structure of the P-space. Element rankings based on Z-contrasts remain highly consistent among model variants ($\rho > 0.95$), while bootstrap analysis confirms the robustness of the principal polar signals.

This indicates that the observed geochemical contrasts reflect not technical features of the compositional transform, but rather a stable organization of the data associated with the state of organic matter.

At the same time, the P-axis should not be interpreted as a binary classifier of "gelified versus non-gelified" states, but rather as a continuous state space. The P-domains represent recurring states of the organic matrix differing in degree of tissue preservation, degree of organic-matter homogenization, and associated geochemical organization.

For this reason, the P-axis is capable of organizing several partially independent subsystems simultaneously:

- elemental geochemistry;
- sulfur-form architecture;
- proximate and ultimate parameters;
- oxide-related subsystems;
- ash-source architecture;
- rank-related features.

In this sense, the P-axis is closer to a coordinate of the internal state of organic matter than to a traditional geochemical proxy.

4.2. Cross-Basin Recurrence: P Is Basin-Conditioned, but Not Basin-Defined

One of the most important outcomes of the study is the cross-basin recurrence of the P-domains. Each of the five global P-domains is represented by multiple basins and countries, whereas the intermediate domain P03 demonstrates particularly broad reproducibility across independent geological systems.

This indicates that the P-space cannot be interpreted as a hidden geographic identifier or a simple function of provenance. Basin conditions clearly influence sample distribution along the P-axis, which is geologically expected for systems with differing histories of peat accumulation, hydrology, and diagenesis. Nevertheless, similar P-states recur across different basins and countries.

The most accurate formulation is therefore:

The P-axis is basin-conditioned, but not basin-defined.

In other words, the P-space reflects reproducible states of organic matter rather than local basin-specific signatures. Similar P-states are observed across independent basins and countries, indicating cross-basin stability of the identified architecture.

Additional support is provided by basin-stratified permutation analysis, which demonstrates preservation of a substantial proportion of P-contrasts even after accounting for basin structure within the dataset. Consequently, the observed P-architecture cannot be reduced to simple geographic clustering.

4.3. The P-Space Does Not Coincide with the Classical Inorganic Fe–S Redox Gradient

At an early stage of the study, the P-axis could potentially have been interpreted as a variant of a classical redox gradient because gelified states are traditionally associated with reducing conditions. However, the obtained results do not support interpretation of the P-axis as a unified inorganic Fe–S redox gradient.

If the P-axis primarily reflected the classical Fe–S redox system, the most stable contrasts should have been observed for:

- pyritic sulfur;
- integrated Fe–S indices;
- U, V, and other classical redox-sensitive elements;
- Fe-bearing mineral-associated signals.

However, this pattern is not observed.

The most stable G-side signals are associated primarily with:

- S_organic;
- bio_organic_sulfur_score;
- biological_vs_inorganic_redox_balance;
- the Sb–Tl–Hg–Cl–Te assemblage.

In contrast:

- S_pyritic;
- inorganic_FeS_redox_score;
- U;
- V;

- Fe_2O_3

display weak, mixed, or statistically unstable signals relative to the P-poles.

Accordingly, the P-space does not coincide with the classical pyritization or aqueous Fe–S system. A more plausible interpretation is that the P-axis organizes several partially independent geochemical subsystems, among which inorganic Fe–S redox represents only one component of the broader architecture.

This distinction is particularly important because the term "redox" in geochemical literature often conflates processes of fundamentally different nature, including:

- tissue preservation;
- sulfur incorporation;
- pyritization;
- pore-water chemistry;
- metal accumulation;
- sulfate reduction;
- fluid-related redistribution.

The present results demonstrate that these processes are not necessarily equivalent or synchronous.

4.4. Biogelification and External Fe–S Geochemical Overprinting

The most important interpretation emerging from the present study is that the P-axis, constructed from the ratio of tissue-preserved and gelified maceral components, primarily records the internal tissue-to-gel transformation of organic matter associated with biochemical and early diagenetic processes.

The P-axis reflects the degree of destruction of the original tissue structure and its transition into a more homogenized organic matrix. This internal transformation is most consistently associated with:

- S_organic;
- bio_organic_sulfur_score;
- the Sb–Tl–Hg–Cl–Te assemblage;
- increasing carbonization-related features;
- reorganization of proximate and ultimate architecture.

In contrast, the inorganic Fe–S subsystem, pyritic sulfur, Fe_2O_3, and part of the classical redox-sensitive elemental assemblage appear to depend more strongly on external geochemical conditions, including:

- sulfate availability;
- iron availability;
- pore-water chemistry;
- fluid influx;
- late-diagenetic and catagenetic processes.

Accordingly, these two systems are not required to form synchronously.

In this sense, the P-axis primarily records the internal state of the organic tissue, whereas inorganic Fe–S proxies may reflect a geochemical subsystem partially independent from, or temporarily decorrelated relative to, the primary tissue-to-gel transformation.

This distinction likely explains why the P-space does not coincide with classical U/V/Mo/S_pyritic proxy systems.

At the same time, the results do not prove a specific microbiological mechanism of gelification or sulfur incorporation. A more appropriate interpretation is that:

- tissue-associated transformation;
- organic sulfur enrichment;
- inorganic Fe–S mineralization

may represent partially independent processes operating within the broader coal system.

4.5. Separation Between Organic Sulfur-Associated and Inorganic Fe–S Subsystems

One of the most robust results of the study is the separation between organic sulfur-associated and inorganic Fe–S-associated signals.

S_organic and bio_organic_sulfur_score are consistently shifted toward G_ref, whereas:

- S_pyritic;
- inorganic_FeS_redox_score;
- Fe_2O_3

do not exhibit stable polar behavior.

Particularly important is the observation that the P-axis correlates positively with:

- S_organic;
- bio_organic_sulfur_score,

but shows no correlation with inorganic_FeS_redox_score.

This indicates that the most stable sulfur-related signal associated with gelified states is linked not to pyritization, but to organically bound sulfur.

At the same time, the present results do not permit direct reconstruction of the mechanism responsible for formation of the organic sulfur subsystem. Such reconstruction would require:

- $\delta^{34}S$ isotope analysis;
- microanalytical sulfur mapping;
- independent diagenetic series;
- experimental models of tissue-to-gel transformation.

Nevertheless, even at the present level of analysis, the observed architecture demonstrates that:

- the organic sulfur subsystem;
- the inorganic Fe–S subsystem

may remain partially independent relative to the P-space.

4.6. Gelification as an Architectural State of Organic Matter

The obtained results indicate that gelification cannot be adequately described through a single element, a single index, or a universal proxy. Instead, the P-axis organizes a coordinated architecture of multiple interconnected subsystems.

The T-side is associated with:

- elevated O, moisture, and volatile matter;
- the lithogenic oxide subsystem;
- the Th–Al–Ba–B–Cr assemblage;
- tissue-preserved signals.

The G-side is characterized by:

- elevated C, fixed carbon, and calorific value;
- increasing rank_proxy_score;
- S_organic-associated signals;
- the Sb–Tl–Hg–Cl–Te fluid/organophilic assemblage.

Most importantly, these features change in a coordinated manner. Therefore, the P-axis reflects not a single chemical process, but rather an integrated state of the organic matrix.

This result is consistent with the nature of coal maceral organization. The transition from tissue-preserved states to gelified matrices likely involves multiple simultaneously operating processes, including:

- dehydration;
- porosity modification;
- redistribution of organic functional groups;
- alteration of mineral-organic interfaces;
- sulfur-related transformations;
- rank-associated changes;
- reorganization of sorption properties.

In this sense, the P-axis is closer to a coordinate of the structural state of organic matter than to a traditional geochemical index.

4.7. Rank and Ash as Subsystems Rather Than Explanations of the Entire Architecture

The obtained results demonstrate that thermal maturity and mineral matter participate in the P-

architecture but do not exhaustively explain it.

The G-side is accompanied by increases in:

- fixed carbon;
- calorific value;
- rank_proxy_score;
- carbon enrichment.

However, many key P-associated elements exhibit only weak relationships with Rmax. Sb, Tl, Te, K, Na, and Bi display pronounced P-signals despite weak or moderate Rmax contrasts. Consequently, the P-axis is partially associated with maturity but is not reducible to it.

Similarly, the P-axis is not reducible to total ash content.

The lithogenic oxide subsystem is consistently shifted toward the T-side, whereas other ash-source subsystems behave differently:

- the Fe–S subsystem exhibits mixed behavior;
- the phosphate subsystem does not form a stable pole;
- the alkali-fluid subsystem behaves independently of total ash content;
- the carbonate subsystem does not exhibit stable contrasts.

Accordingly, ash cannot be interpreted as a single controlling factor. Instead, the mineral component of coal represents a multicomponent architecture of partially independent subsystems.

4.8. Why Single-Proxy Approaches Become Unstable

The present results help explain why the search for universal geochemical proxies of gelification remains unstable.

Petrographic gelification is expressed not through a single universal element or elemental ratio, but through the coordinated architecture of several partially independent subsystems:

- P-state;
- rank;
- lithogenic framework;
- S_organic subsystem;
- inorganic Fe–S subsystem;
- fluid-associated components;
- ash-source architecture.

Within such a system, the behavior of individual elements may vary depending on which subsystem dominates within a given sample.

Consequently, attempts to describe gelification using isolated proxies inevitably lead to basin-specific

or unstable results.

The present study suggests that a more productive approach may involve analysis of state architectures rather than the search for a single universal indicator element.

4.9. Limitations of the Study

Despite the robustness of the identified patterns, the present study has several limitations.

First, the proposed P-space represents a calibrated state-space framework constructed on the current WoCQI-derived dataset. Its robustness was evaluated through sensitivity analysis, bootstrap resampling, alternative P-models, lithogenic-background testing, and basin-stratified permutation, rather than through an independent test-set in the predictive-model sense. Accordingly, further validation should not be understood as testing against a separate "external dataset" alone, but rather as progressive expansion of the calibration space by incorporating additional basins, maturity ranges, depositional settings, and coal-system types. In this sense, the proposed P-space should be regarded as an evolving coordinate framework whose stability depends on adequate coverage of the multidimensional state-space of organic matter.

Second, the process-space coordinates represent operational descriptors rather than direct measurements of geological mechanisms. Accordingly, terms such as redox, sulfur subsystem, fluid-associated assemblage, or lithogenic subsystem should be interpreted as architectural subsystems rather than uniquely defined causal processes.

Third, the study does not include:

- sulfur isotope analysis;
- microanalytical sulfur mapping;
- experimental models of tissue-to-gel transformation;
- direct dating of sulfur-related processes.

Therefore, the proposed separation between organic sulfur-associated and inorganic Fe–S-associated subsystems should be regarded as an architectural interpretation requiring further validation through isotopic, microanalytical, and experimental approaches.

Finally, several elements contributing to the G-side assemblage (particularly Te, Bi, and Be) are represented by relatively limited numbers of measurements above detection limits. Although bootstrap and sensitivity analyses indicate stability of the major architectural patterns, additional datasets would further refine the role of these trace-element associations within the proposed P-space framework.

4.10. Final Interpretation

Taken together, the results demonstrate that the P-axis defines a stable and cross-basin reproducible space of organic matter states accompanied by coordinated reorganization of multiple geochemical subsystems.

The most important conclusions are:

- the P-space does not coincide with a single inorganic Fe–S redox gradient;
- organic sulfur-associated and inorganic Fe–S-associated signals may diverge;
- the P-axis primarily reflects the internal state of the organic matrix;
- rank and ash participate in the overall architecture but do not fully explain it.

In this sense, the P-axis may be interpreted as a coordinate of tissue-to-gel organization of organic matter around which several partially independent geochemical subsystems are organized.

5. CONCLUSIONS

The present study demonstrates that a petrographic P-axis constructed exclusively from the ratio of tissue-preserved and gelified vitrinite components can be regarded as an independent coordinate of coal organic matter state. Unlike traditional single-proxy approaches, the P-axis does not rely on geochemical variables and is not predetermined by a selected redox model, but instead reflects the internal tissue-to-gel organization of the organic matrix.

The obtained results demonstrate that multiple partially independent geochemical subsystems are reproducibly organized around the P-axis, including element-associated architecture, sulfur-form organization, proximate and ultimate parameters, oxide-related subsystems, ash-source components, and rank-related features. Importantly, the identified architecture remains stable under changes in P-model parameterization, alternative lithogenic backgrounds, and bootstrap resampling, indicating the robustness of the P-space and the independence of the principal conclusions from technical parameterization.

The study further demonstrates that P-domains recur across basins and countries. Accordingly, the P-axis is basin-conditioned, but not basin-defined: sample positions along the P-axis are influenced by basin conditions, yet similar P-states recur across independent geological systems and cannot be reduced to simple basin affiliation.

The most important result of the study is that the P-space does not coincide with the classical inorganic Fe–S-associated redox gradient. The most stable G-side signals are associated primarily with S_organic, bio_organic_sulfur_score, and the Sb–Tl–Hg–Cl–Te assemblage, whereas S_pyritic, inorganic_FeS_redox_score, U, V, and Fe-bearing indicators display weak, mixed, or statistically unstable relationships relative to the P-poles. Accordingly, organic sulfur-associated and inorganic Fe–S-associated subsystems may become partially decoupled within the broader coal system.

The obtained results support the interpretation that the P-axis primarily records the internal tissue-to-gel transformation of organic matter and the associated reorganization of the organic matrix, whereas part of the inorganic Fe–S-related signal is controlled by additional external geochemical factors, including iron and sulfate availability, pore-water chemistry, fluid influx, and late-diagenetic processes.

The study additionally demonstrates that the P-axis is reducible neither to thermal maturity nor to total

ash content. Although rank-related and ash-related features participate in the overall P-space architecture, they do not fully explain it. Maturity, lithogenic components, sulfur-related organization, and fluid-associated signatures together form a multicomponent system of partially independent coordinates.

Accordingly, gelification of organic matter cannot be adequately described through a single element, a single index, or a universal redox proxy. A more appropriate interpretation is to regard the P-space as a multidimensional process-space architecture in which tissue preservation, gelification, organic sulfur enrichment, inorganic Fe–S mineralization, rank evolution, and ash-source organization interact without being fully equivalent or synchronous processes.

Overall, the study demonstrates that an architectural approach to analysis of organic matter state makes it possible to move beyond unstable single-proxy indicators toward investigation of stable multidimensional state configurations. In this context, the petrographic P-axis may be regarded as a reproducible coordinate of the internal state of the organic matrix suitable for cross-basin comparison, process-space calibration, and further development of multidimensional models of coal geochemistry.

6. Data and Code Availability

The complete source code, calibration files, result tables, supplementary figures, and supporting materials used in this study are publicly available through Zenodo at:

https://doi.org/10.5281/zenodo.20440805

7. Acknowledgements

The author gratefully acknowledges the WoCQI professional community for discussions related to coal geochemistry, petrographic interpretation, and multidimensional analytical approaches to coal quality assessment.

References

Aitchison, J., 1986. The Statistical Analysis of Compositional Data. Chapman & Hall, London.

Amrani, A., 2014. Organic sulfur in the geosphere: analysis, structures and chemical processes. In: Turekian, K.K., Holland, H.D. (Eds.), Treatise on Geochemistry, second ed., vol. 12. Elsevier, pp. 291-333. https://doi.org/10.1016/B978-0-08-095975-7.00920-1

Casagrande, D.J., 1987. Sulfur in peat and coal. In: Scott, A.C. (Ed.), Coal and Coal-bearing Strata: Recent Advances. Geological Society of London Special Publication 32, 87-105.

Chou, C.-L., 2012. Sulfur in coals: A review of geochemistry and origins. International Journal of Coal Geology 100, 1-13. https://doi.org/10.1016/j.coal.2012.05.009

Dai, S., Bechtel, A., Eble, C.F., Flores, R.M., French, D., Graham, I.T., Hood, M.M., Hower, J.C., Korasidis, V.A., Moore, T.A., Püttmann, W., Wei, Q., Zhao, L., O'Keefe, J.M.K., 2020. Recognition of peat depositional environments in coal: A review. International Journal of Coal Geology 219, 103383. https://doi.org/10.1016/j.coal.2019.103383

Diessel, C.F.K., 1992. Coal-Bearing Depositional Systems. Springer-Verlag. https://doi.org/10.1007/978-3-642-75668-9

Efron, B., Tibshirani, R.J., 1993. An Introduction to the Bootstrap. Chapman & Hall/CRC, New York.

Epshtein, S.A., Kossovich, E.L., Kaminskii, V.A., Durov, N.M., Dobryakova, N.N., 2017. Solid fossil fuels thermal decomposition features in air and argon. Fuel 199, 145-156. https://doi.org/10.1016/j.fuel.2017.02.029

Epshtein, S.A., Shkuratnik, V.L., Kossovich, E.L., Agarkov, K.V., Nesterova, V.G., Gavrilova, D.I., 2020. Effects of cyclic freezing and thawing of coals at their behavior at low- and high-temperature oxidation. Fuel 267, 117191. https://doi.org/10.1016/j.fuel.2020.117191

Filzmoser, P., Hron, K., Templ, M., 2018. Applied Compositional Data Analysis. Springer, Cham. https://doi.org/10.1007/978-3-319-96422-5

Finkelman, R.B., Lovern, V.S., 2001. The World Coal Quality Inventory (WoCQI). U.S. Geological Survey Fact Sheet 155-00. https://doi.org/10.3133/fs15500

Hower, J.C., Eble, C.F., 1996. Petrology, palynology and geochemistry of the Stockton coal bed (Middle Pennsylvanian) in eastern Kentucky. In: Flint, S.S., Bryant, I.D. (Eds.), Geological Society of America Special Paper 308, 41-54.

Hower, J.C., Ruppert, L.F., Eble, C.F., 1994. Petrology, palynology, and geochemistry of the Pond Creek coal bed (Middle Pennsylvanian) in eastern Kentucky. International Journal of Coal Geology 25(3-4), 243-277.

Jochum, K.P., Nohl, U., 2008. Reference materials in geochemistry and environmental research and the GeoReM database. Chemical Geology 253(1-2), 50-53. https://doi.org/10.1016/j.chemgeo.2008.04.002

Jones, B., Manning, D.A.C., 1994. Comparison of geochemical indices used for the interpretation of palaeoredox conditions in ancient mudstones. Chemical Geology 111(1-4), 111-129.

Kane, J.S., 1992. Reference samples for use in analytical geochemistry: their availability, preparation, and appropriate use. Journal of Geochemical Exploration 44(1-3), 37-63. https://doi.org/10.1016/0375-6742(92)90047-C

Pawlowsky-Glahn, V., Egozcue, J.J., Tolosana-Delgado, R., 2015. Modeling and Analysis of Compositional Data. John Wiley & Sons, Chichester. https://doi.org/10.1002/9781119003144

Ruebsam, W., Dickson, A.J., Hoyer, E.-M., Schwark, L., 2017. Multiproxy reconstruction of oceanographic conditions in the southern epeiric Kupferschiefer Sea (Late Permian) based on redox-sensitive trace elements, molybdenum

isotopes and biomarkers. Gondwana Research 44, 205-218. https://doi.org/10.1016/j.gr.2016.12.012

Sen, S., 2016a. Discussion on the concepts in paleoenvironmental reconstruction from coal macerals and petrographic indices. Marine and Petroleum Geology 73, 371-391.

Sen, S., 2016b. Review on coal petrographic indices and models and their applicability in paleoenvironmental interpretation. Journal of the Geological Society of India 87(6), 719-729.

Schagarova, O., 2025. P-axis coal geochemistry framework: source code, calibration files and supplementary materials (Version 1.0). Zenodo. https://doi.org/10.5281/zenodo.20440805

Teichmüller, M., 1989. The genesis of coal from the viewpoint of coal geology. In: Lyons, P.C., Alpern, B. (Eds.), Peat and Coal: Origin, Facies, and Depositional Models. International Journal of Coal Geology 12(1-4), 1-87.

Teichmüller, M., 1990. Die Genese der Kohle aus kohlenpetrologischer Sicht. Fortschritte in der Geologie von Rheinland und Westfalen 36, 7-66.

Tewalt, S.J., Bragg, L.J., Finkelman, R.B., 2006. The World Coal Quality Inventory: South America. U.S. Geological Survey Open-File Report 2006-1241. https://doi.org/10.3133/ofr20061241